



The MOSDEF Survey: Sulfur Emission-line Ratios Provide New Insights into Evolving Interstellar Medium Conditions at High Redshift*

Alice E. Shapley¹ , Ryan L. Sanders² , Peng Shao³, Naveen A. Reddy⁴ , Mariska Kriek⁵ , Alison L. Coil⁶ , Bahram Mobasher⁴, Brian Siana⁴ , Irene Shivarai^{7,12} , William R. Freeman⁴ , Mojegan Azadi⁸ , Sedona H. Price⁹ , Gene C. K. Leung⁶ , Tara Fetherolf⁴, Laura de Groot¹⁰, Tom Zick⁵, Francesca M. Fornasini⁸ , and Guillermo Barro¹¹

¹Department of Physics and Astronomy, University of California, Los Angeles, 430 Portola Plaza, Los Angeles, CA 90095, USA; aes@astro.ucla.edu

²Department of Physics, University of California, Davis, 1 Shields Avenue, Davis, CA 95616, USA

³School of Astronomy and Space Science, Nanjing University, Nanjing 210023, People's Republic of China

⁴Department of Physics and Astronomy, University of California, Riverside, 900 University Avenue, Riverside, CA 92521, USA

⁵Astronomy Department, University of California at Berkeley, Berkeley, CA 94720, USA

⁶Center for Astrophysics and Space Sciences, Department of Physics, University of California, San Diego, 9500 Gilman Drive, La Jolla, CA 92093, USA

⁷Steward Observatory, University of Arizona, 933 North Cherry Avenue, Tucson, AZ 85721, USA

⁸Harvard-Smithsonian Center for Astrophysics, 60 Garden Street, Cambridge, MA, 02138, USA

⁹Max-Planck-Institut für Extraterrestrische Physik, Postfach 1312, Garching, D-85741, Germany

¹⁰Department of Physics, The College of Wooster, 1189 Beall Avenue, Wooster, OH 44691, USA

¹¹Department of Physics, University of the Pacific, 3601 Pacific Avenue, Stockton, CA 95211, USA

Received 2019 July 15; revised 2019 August 1; accepted 2019 August 5; published 2019 August 20

Abstract

We present results on the emission-line properties of $1.3 \leq z \leq 2.7$ galaxies drawn from the complete the MOSFIRE Deep Evolution Field (MOSDEF) survey. Specifically, we use observations of the emission-line diagnostic diagram of $[\text{O III}]\lambda 5007/\text{H}\beta$ versus $[\text{S II}]\lambda\lambda 6717, 6731/\text{H}\alpha$, i.e., the “[S II] BPT diagram,” to gain insight into the physical properties of high-redshift star-forming regions. High-redshift MOSDEF galaxies are offset toward lower $[\text{S II}]\lambda\lambda 6717, 6731/\text{H}\alpha$ at fixed $[\text{O III}]\lambda 5007/\text{H}\beta$, relative to local galaxies from the Sloan Digital Sky Survey (SDSS). Furthermore, at fixed $[\text{O III}]\lambda 5007/\text{H}\beta$, local SDSS galaxies follow a trend of decreasing $[\text{S II}]\lambda\lambda 6717, 6731/\text{H}\alpha$ as the surface density of star formation (Σ_{SFR}) increases. We explain this trend in terms of the decreasing fractional contribution from diffuse ionized gas (f_{DIG}) as Σ_{SFR} increases in galaxies, which causes galaxy-integrated line ratios to shift toward the locus of pure H II-region emission. The $z \sim 0$ relationship between f_{DIG} and Σ_{SFR} implies that high-redshift galaxies have lower f_{DIG} values than typical local systems, given their significantly higher typical Σ_{SFR} . When an appropriate low-redshift benchmark with zero or minimal f_{DIG} is used, high-redshift MOSDEF galaxies appear offset toward higher $[\text{S II}]\lambda\lambda 6717, 6731/\text{H}\alpha$ and/or $[\text{O III}]\lambda 5007/\text{H}\beta$. The joint shifts of high-redshift galaxies in the [S II] and [N II] BPT diagrams are best explained in terms of the harder spectra ionizing their star-forming regions at fixed nebular oxygen abundance (expected for chemically young galaxies), as opposed to large variations in N/O ratios or higher ionization parameters. The evolving mixture of H II regions and diffuse ionized gas is an essential ingredient of our description of the interstellar medium over cosmic time.

Unified Astronomy Thesaurus concepts: [High-redshift galaxies \(734\)](#); [Interstellar medium \(847\)](#); [Galaxy evolution \(594\)](#)

1. Introduction

Rest-optical emission-line ratios provide a powerful probe of the physical conditions in the interstellar medium (ISM). Local star-forming galaxies trace a tight sequence of increasing $[\text{N II}]\lambda 6584/\text{H}\alpha$ and decreasing $[\text{O III}]\lambda 5007/\text{H}\beta$, as metallicity increases and the overall excitation in star-forming regions decreases. Recent statistical samples of rest-optical spectra of $z \sim 2$ galaxies show that high-redshift galaxies are offset systematically from local galaxies toward higher $[\text{O III}]\lambda 5007/\text{H}\beta$ and $[\text{N II}]\lambda 6584/\text{H}\alpha$ values on average (Steidel et al. 2014; Shapley et al. 2015). There are many possible causes for this observed difference in $z \sim 2$ galaxies, including higher ionization parameters in distant H II regions, harder ionizing spectra at fixed metallicity for the stars photoionizing the H II

regions, higher densities (or equivalently pressures), variations in the gas-phase N/O abundance patterns, and contributions from active galactic nuclei (AGNs) and shocks (e.g., Masters et al. 2014; Coil et al. 2015; Sanders et al. 2016; Steidel et al. 2016; Kashino et al. 2017; Freeman et al. 2019).

The differences between high-redshift and local emission-line sequences were first noted in the $[\text{O III}]\lambda 5007/\text{H}\beta$ versus $[\text{N II}]\lambda 6584/\text{H}\alpha$ diagnostic diagram, i.e., the so-called [N II] Baldwin, Phillips & Terlevich (BPT) diagram (Baldwin et al. 1981). However, in interpreting these differences, various authors have considered the properties of galaxies in the $[\text{O III}]\lambda 5007/\text{H}\beta$ versus $[\text{S II}]\lambda\lambda 6717, 6731/\text{H}\alpha$ diagram (first introduced in Veilleux & Osterbrock 1987, and referred to hereafter as the “[S II] BPT diagram”) and the space of $[\text{O III}]\lambda\lambda 4959, 5007/[\text{O II}]\lambda\lambda 3726, 3729$ (O_{32}) versus $([\text{O III}]\lambda\lambda 4959, 5007 + [\text{O II}]\lambda\lambda 3726, 3729)/\text{H}\beta$ (R_{23}). The lack of a significant positive offset in the [S II] BPT and O_{32} versus R_{23} diagrams has been used to argue that $z \sim 0$ and $z \sim 2$ galaxies follow different N/O abundance patterns (Masters et al. 2014; Shapley et al. 2015). A small positive offset measured in the

* Based on data obtained at the W.M. Keck Observatory, which is operated as a scientific partnership among the California Institute of Technology, the University of California, and the National Aeronautics and Space Administration, and was made possible by the generous financial support of the W.M. Keck Foundation.

¹² Hubble Fellow.

[S II] BPT diagram has been used to suggest a harder ionizing spectrum at fixed nebular abundance (Steidel et al. 2016; Strom et al. 2017) at $z \sim 2$. Meanwhile, a *negative* offset in [S II] $\lambda\lambda 6717, 6731/H\alpha$ at fixed [O III] $\lambda 5007/H\beta$ for $z \sim 1.5$ star-forming galaxies has been attributed to a higher ionization parameter (Kashino et al. 2017, 2019).

While arriving at different conclusions regarding the evolution of the properties of star-forming regions at high redshift, the analyses of local and high-redshift emission-line diagnostic diagrams typically share a common approach. Specifically, integrated slit or fiber spectra of distant galaxies are compared with fiber spectra of local galaxies drawn from the Sloan Digital Sky Survey (SDSS; Abazajian et al. 2009). Each galaxy is effectively represented as a point source, when in fact the integrated spectrum of a galaxy contains the sum of the emission from the ensemble of H II regions that fall within the spectral aperture, along with the contribution from diffuse ionized gas (DIG) in the ISM. DIG exists outside H II regions, and has been shown to contribute typically 30%–60% of the total $H\alpha$ flux in local spiral galaxies (Zurita et al. 2000; Oey et al. 2007). Furthermore, the fractional contribution of DIG emission to the Balmer lines declines with increasing star formation rate (SFR) surface density (Σ_{SFR} ; Oey et al. 2007). Zhang et al. (2017) and Sanders et al. (2017) have also demonstrated that distinct physical conditions and ionizing spectra in the DIG and H II regions result in systematically different DIG and H II region excitation sequences in emission-line diagrams featuring [S II] or [O II], while not strongly affecting the [N II] BPT diagram. Clearly, a robust interpretation of the evolving internal properties of H II regions with increasing redshift requires an understanding of the evolving mixture of DIG and H II regions within star-forming galaxies.

In this work, we examine how the different mixtures of DIG and H II region emission at low and high redshifts affect inferences regarding the evolution of H II region properties out to $z \sim 2$. We analyze galaxies at $1.3 \leq z \leq 2.7$ drawn from the MOSFIRE Deep Evolution Field (MOSDEF) survey (Kriek et al. 2015) in comparison with local SDSS galaxies. Most importantly, we consider the implications of the fact that Σ_{SFR} is typically two orders of magnitude higher in star-forming galaxies at $z \sim 2$, compared with $z \sim 0$ galaxies. In Section 2, we describe our observations and samples. In Section 3, we revisit the comparison between local and high-redshift emission-line diagrams, accounting for their additional differences in Σ_{SFR} . In Section 4, we discuss the implications for inferring the internal properties of high-redshift star-forming regions. Throughout, we adopt cosmological parameters of $H_0 = 70 \text{ km s}^{-1} \text{ Mpc}^{-1}$, $\Omega_m = 0.30$, and $\Omega_\Lambda = 0.7$, and a Chabrier (2003) initial mass function (IMF).

2. Observations and Samples

2.1. MOSDEF Survey and Sample

Our analysis is based on the complete MOSDEF survey data set. Full details of the survey observations and data reduction are provided in Kriek et al. (2015). In brief, MOSDEF was a 48.5-night observing program over 4 yr using Multi-Object Spectrometer for Infra-Red Exploration (MOSFIRE; McLean et al. 2012) on the 10 m Keck I telescope. With MOSDEF, we obtained rest-optical spectra for a sample of ~ 1500 galaxies at $1.4 \leq z \leq 3.8$ in the COSMOS, GOODS-N, AEGIS, GOODS-S, and UDS fields covered by the CANDELS

and 3D-*HST* surveys (Grogin et al. 2011; Koekemoer et al. 2011; Momcheva et al. 2016). These fields are covered by extensive multi-wavelength observations (e.g., Skelton et al. 2014). MOSDEF targets fall within three distinct redshift intervals, where the strongest rest-optical emission lines are accessible through windows of atmospheric transmission: $1.37 \leq z \leq 1.70$, $2.09 \leq z \leq 2.61$, and $2.95 \leq z \leq 3.80$. Here we focus on galaxies in the two lower-redshift intervals, hereafter described as $z \sim 1.5$ and $z \sim 2.3$, for which not only [O II] $\lambda\lambda 3726, 3729$, $H\beta$, [O III] $\lambda\lambda 4959, 5007$ are accessible from the ground, but also $H\alpha$, [N II] $\lambda 6584$, and [S II] $\lambda\lambda 6717, 6731$.

In addition to measurements of strong rest-optical nebular emission lines for MOSDEF galaxies, we also analyze dust-corrected $H\alpha$ star formation surface densities, i.e., Σ_{SFR} . To obtain Σ_{SFR} , we determined nebular extinction, $E(B - V)_{\text{neb}}$, from the stellar-absorption-corrected $H\alpha/H\beta$ Balmer decrement and the assumption of the Milky Way dust extinction curve (Cardelli et al. 1989). $H\alpha$ SFRs ($\text{SFR}(H\alpha)$) were then estimated from dust-corrected and slit-loss-corrected $H\alpha$ luminosities, based on the calibration of Hao et al. (2011) for a Chabrier (2003) IMF. The procedures for stellar-absorption, dust, and slit-loss corrections are fully described in Reddy et al. (2015) and Kriek et al. (2015). We also require galaxy sizes for Σ_{SFR} . van der Wel et al. (2014) fit single-component Sérsic profiles to the two-dimensional light distributions of galaxies in the CANDELS fields, and derive half-light radii, r_e , as the semimajor axis of the ellipse containing half of the total galaxy light. We use F160W galaxy half-light radii from the publicly available catalogs of Wel et al., and then define SFR surface density as

$$\Sigma_{\text{SFR}} = \frac{\text{SFR}(H\alpha)}{2\pi r_e^2}. \quad (1)$$

Our main analysis is based on samples of MOSDEF galaxies at $z \sim 1.5$ and $z \sim 2.3$ with coverage of the $H\beta$, [O III], $H\alpha$, [N II], and [S II] emission lines. Specifically, we selected 434 [211] galaxies at $2.0 \leq z \leq 2.7$ [$1.3 \leq z \leq 1.7$], with robust spectroscopic redshifts, $S/N \geq 3$ in $H\alpha$ emission-line flux, and no evidence for active galactic nucleus (AGN) activity based on X-ray luminosity, *Spitzer*/IRAC colors, or [N II] $\lambda 6584/H\alpha$ ratios (Coil et al. 2015; Azadi et al. 2017). The $z \sim 2.3$ sample is characterized by a median redshift and stellar mass of $z_{\text{med}} = 2.28$ and $\log(M/M_\odot)_{\text{med}} = 9.92$, respectively, while the corresponding values for the $z \sim 1.5$ sample are $z_{\text{med}} = 1.52$ and $\log(M/M_\odot)_{\text{med}} = 9.95$.

2.2. SDSS $z \sim 0$ Comparison Sample

In order to gain insights into the evolving properties of star-forming regions at high redshift, we selected a comparison sample of local galaxies from the SDSS Data release 7 (DR7; Abazajian et al. 2009). Stellar-absorption-corrected emission-line measurements are drawn from the MPA-JHU catalog of measurements for DR7,¹³ as well as the corrections needed to correct fiber to total emission-line fluxes. In order to estimate Σ_{SFR} for SDSS galaxies, we calculated $E(B - V)_{\text{neb}}$, dust-corrected $H\alpha$ luminosities, and $\text{SFR}(H\alpha)$ for SDSS galaxies using the methodology described above. In analogy with the rest-optical half-light radii adopted for MOSDEF galaxies, we used the elliptical Petrosian R -band half-light radii for SDSS

¹³ Available at <http://www.mpa-garching.mpg.de/SDSS/DR7/>.

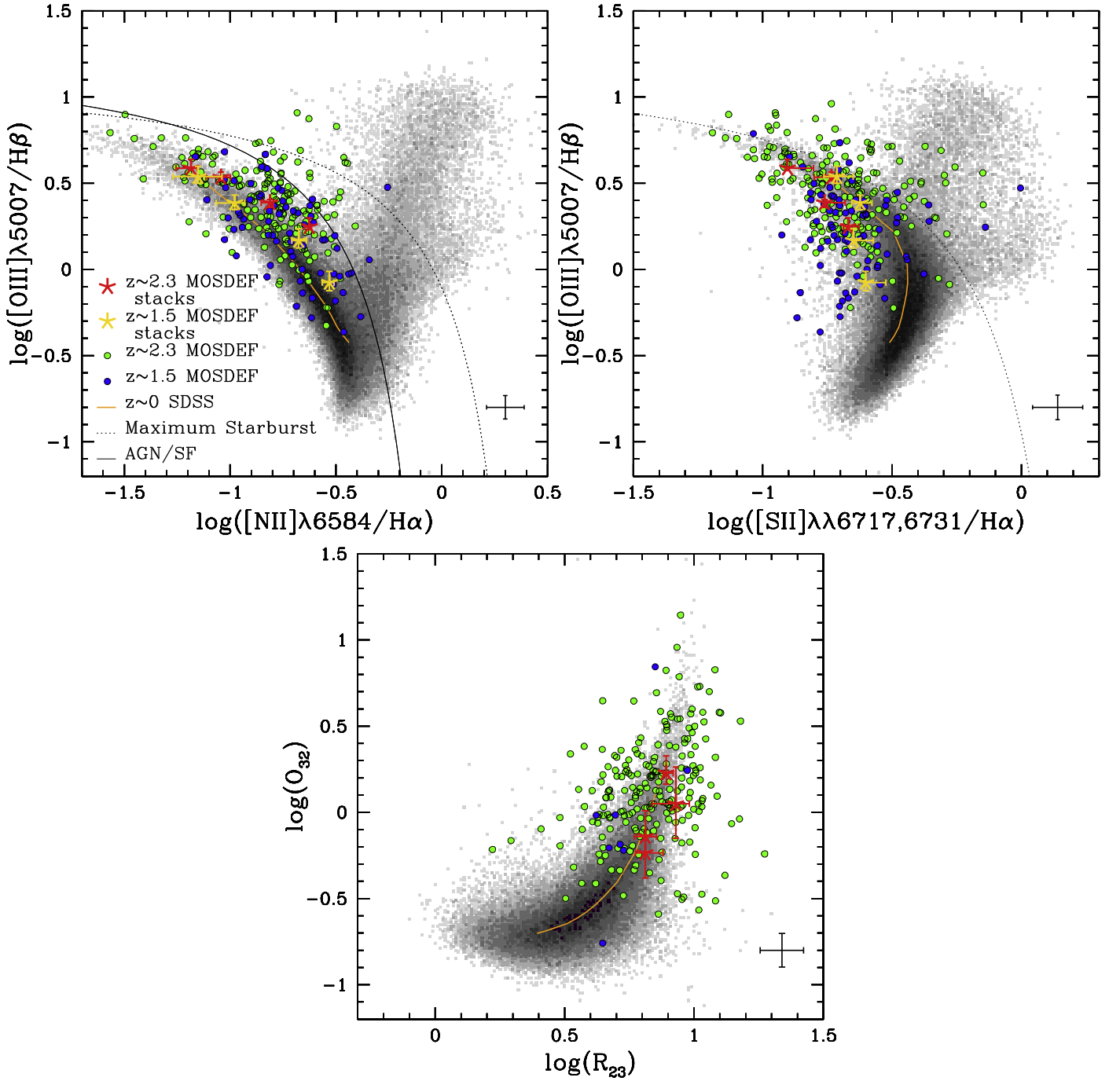


Figure 1. Top-left panel: [N II] BPT diagram for $1.4 \leq z \leq 2.7$ MOSDEF galaxies. Green [blue] points indicate $z \sim 2.3$ [$z \sim 1.5$] MOSDEF galaxies with $\geq 3\sigma$ detections of all four BPT emission lines. Median MOSDEF error bars are indicated in the lower right-hand corner of each panel. The grayscale histogram and orange curve correspond, respectively, to the distribution and running median of local SDSS galaxies. The running median line ratios are calculated in closely spaced bins of stellar mass. Large red [gold] stars indicate measurements from composite spectra, binned by stellar mass, of all MOSDEF $z \sim 2.3$ [$z \sim 1.5$] galaxies with coverage of the relevant emission lines and $\geq 3\sigma$ $H\alpha$ detections. Stacks of increasing stellar mass have lower $[O III]\lambda 5007/H\beta$. The black dotted curve is the “maximum starburst” line from Kewley et al. (2001), while the black solid curve is an empirical AGN/star formation threshold from Kauffmann et al. (2003). Although plotted here for completeness, SDSS galaxies falling above the Kauffmann et al. (2003) curve are not included in our analysis. Top-right panel: [S II] BPT diagram. Symbols are the same as in the top-left panel. Bottom panel: O_{32} vs. R_{23} diagram, corrected for dust. Stacked points are not shown for the $z \sim 1.5$ sample in this panel, given the small size of the sample with $[O II]\lambda\lambda 3726, 3729$ coverage.

galaxies drawn from the NASA-Sloan Atlas v1.0.1,¹⁴ and applied Equation (1) to obtain Σ_{SFR} . We restricted the SDSS sample to galaxies at $0.04 \leq z \leq 0.10$ to reduce aperture

effects, and required 5σ detections for all lines included in the [S II] and [N II] BPT diagrams (i.e., $H\beta$, $[O III]$, $H\alpha$, [N II], and [S II]). As we wish to study the star formation properties of the SDSS sample, we also removed galaxies from our analysis that satisfied the optical emission-line AGN criterion of Kauffmann et al. (2003). We finally required a robust half-light radius

¹⁴ Available at <http://www.nsatlas.org>.

entry in the NASA-Sloan Atlas. The above criteria yielded a $z \sim 0$ comparison sample of 60,609 SDSS galaxies with $\log(M/M_{\odot})_{\text{med}} = 9.83$.

3. Emission-line Ratios at Low and High Redshift

3.1. MOSDEF Emission-line Diagrams

We present here a significantly expanded sample of $z \sim 2.3$ rest-optical emission-line ratio measurements compared to our previous work (Shapley et al. 2015; Sanders et al. 2016), now based on the completed MOSDEF survey. In addition, for the first time we present the same set of measurements for the $z \sim 1.5$ MOSDEF sample. Figure 1 shows MOSDEF galaxies in the [N II] and [S II] BPT diagrams, as well as O_{32} versus R_{23} . Of the galaxies in the [N II] and [S II] BPT samples with coverage of all BPT features and detections of $H\alpha$ emission, there are 179 [68] objects with all [N II] BPT features individually detected at $\geq 3\sigma$ significance at $z \sim 2.3$ [$z \sim 1.5$]. The $z \sim 2.3$ [$z \sim 1.5$] sample size with all features detected in the [S II] BPT diagram is 201 [79]. For the O_{32} versus R_{23} diagram the number of galaxies with [O II], $H\beta$, [O III], and $H\alpha$ detected is 224 [8] at $z \sim 2.3$ [$z \sim 1.5$]. In each of the 3 panels of Figure 1, we show not only the subset of individual detections, but measurements from median stacked spectra from the full sample of MOSDEF galaxies in bins of stellar mass, constructed as described in Sanders et al. (2018).

Based on the full MOSDEF sample, we recover the well-known offset for $z > 1$ galaxies in the [N II] BPT diagram, toward higher [N II] $\lambda 6584/H\alpha$ and [O III] $\lambda 5007/H\beta$ relative to the sequence of $z \sim 0$ star-forming galaxies. In detail, the $z \sim 2.3$ MOSDEF sample appears to be slightly more offset than the $z \sim 1.5$ sample. In the [S II] BPT diagram, the spectral stacks reveal the average trend for $z \geq 1.3$ MOSDEF galaxies is offset from the local sequence toward lower [S II] $\lambda\lambda 6717, 6731/H\alpha$ at fixed [O III] $\lambda 5007/H\beta$, which is consistent with the results of Kashino et al. (2017, 2019). In the O_{32} versus R_{23} diagram, we highlight the results from $z \sim 2.3$, because the $z \sim 1.5$ sample contains few objects with coverage of [O II] $\lambda\lambda 3726, 3729$. Spectral stacks show that the $z \sim 2.3$ sequence is slightly offset toward higher R_{23} at fixed O_{32} , relative to the local sequence. In the discussion that follows, we focus on the [S II] BPT diagram in more detail.

3.2. Σ_{SFR} and the [S II] BPT Diagram

In order to understand the emission-line properties of high-redshift galaxies, we turn to the local [S II] BPT diagram, considering the connection between the location in this diagram and Σ_{SFR} . As previously featured in Masters et al. (2016), Figure 2 shows a clear trend toward lower [S II] $\lambda\lambda 6717, 6731/H\alpha$ at fixed [O III] $\lambda 5007/H\beta$ as Σ_{SFR} increases. We now explain this trend based on the result from Oey et al. (2007), according to which the fraction of the Balmer flux contributed by DIG, f_{DIG} , is a decreasing function of the dust-corrected $H\alpha$ surface brightness—or, equivalently, Σ_{SFR} . Recasting the fit from Sanders et al. (2017) to the Oey et al. data in terms of Σ_{SFR} , we find

$$f_{\text{DIG}} = -0.900 \times \left(\frac{\Sigma_{\text{SFR}}}{M_{\odot} \text{yr}^{-1} \text{kpc}^{-2}} \right)^{1/3} + 0.748. \quad (2)$$

Accordingly, galaxies with higher Σ_{SFR} have lower f_{DIG} . In addition to showing the [O III] $\lambda 5007/H\beta$ versus [S II] $\lambda\lambda 6717, 6731/H\alpha$ locus for SDSS galaxies, Figure 2 also features the corresponding median sequence for local H II

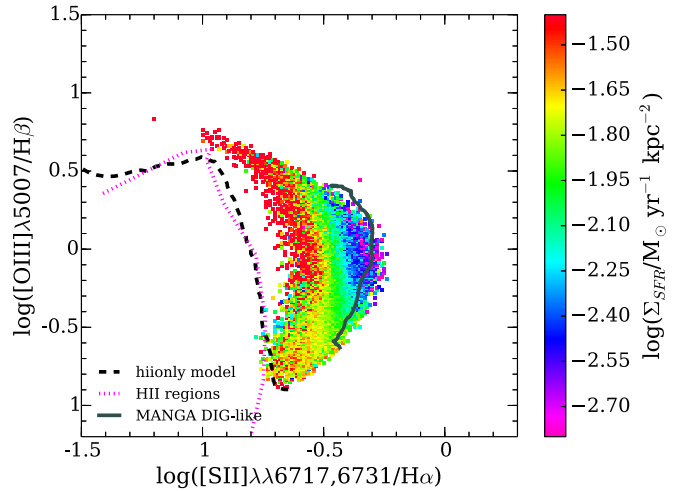


Figure 2. Median Σ_{SFR} for SDSS galaxies as a function of position in the [S II] BPT diagram. There is a strong trend for galaxies with higher values of Σ_{SFR} to be shifted toward lower values of [S II] $\lambda\lambda 6717, 3731/H\alpha$ at fixed [O III] $\lambda 5007/H\beta$ (Masters et al. 2016). In addition, we indicate the running median for local H II regions (Pilyugin & Grebel 2016) with the dotted pink line. The running median line ratios are calculated in bins of H II-region electron temperature. The *hionly* model from Sanders et al. (2017) is shown with the dashed black line, representing the ensemble average emission from H II regions in star-forming galaxies in the absence of DIG emission. Finally, the running median for “DIG”-like (i.e., low $H\alpha$ surface brightness) spaxels from the SDSS/MaNGA DIG galaxy sample used in Sanders et al. (2017) is shown as the solid dark-gray curve. The running median line ratios for the “DIG”-like curve are calculated in bins of $([\text{O III}]\lambda 5007/H\beta)/([\text{N II}]\lambda 6584/H\alpha)$, which correlates with nebular metallicity in local H II regions (Pettini & Pagel 2004).

regions drawn from the sample of Pilyugin & Grebel (2016), and that traced out by the *hionly* model from Sanders et al. (2017). The *hionly* model represents the ensemble average emission from H II regions in star-forming galaxies, and does not include DIG emission. Figure 2 also shows the median sequence for DIG-dominated spaxels from galaxies in the SDSS MaNGA survey (Zhang et al. 2017). The H II region sequences are offset toward significantly lower [S II] $\lambda\lambda 6717, 6731/H\alpha$ at fixed [O III] $\lambda 5007/H\beta$, relative to SDSS galaxies, while the DIG-dominated spaxels are shifted toward higher [S II] $\lambda\lambda 6717, 6731/H\alpha$. It is worth noting that the same segregation between H II region, SDSS galaxy, and DIG emission sequences is not apparent in the [N II] BPT diagram (Sanders et al. 2017; Zhang et al. 2017). It is clear that, as Σ_{SFR} increases and f_{DIG} decreases, the [O III] $\lambda 5007/H\beta$ versus [S II] $\lambda\lambda 6717, 6731/H\alpha$ locus of SDSS galaxies shifts toward the H II region sequence (or, equivalently, the *hionly* model, which excludes the contribution of DIG emission).

3.3. Σ_{SFR} at Low and High Redshift

At $z > 1$, star-forming galaxies of the same stellar mass have significantly higher SFRs and smaller radii. The combination of these factors results in dramatically different median values of Σ_{SFR} for the MOSDEF samples presented here, compared with the properties of $z \sim 0$ SDSS galaxies. In Figure 3, we show the distribution of Σ_{SFR} for our $z \sim 0$ SDSS comparison sample (black histogram), as well as the corresponding distributions for the $z \sim 2.3$ and $z \sim 1.5$ MOSDEF samples (green and blue shaded histograms, respectively). The median $\log(\Sigma_{\text{SFR}})$ values at $z \sim 0$, 1.5, and 2.3 are -1.93 , -0.46 , and -0.03 , where Σ_{SFR} is in units of $M_{\odot} \text{yr}^{-1} \text{kpc}^{-2}$. Therefore, the difference in typical Σ_{SFR} at $z \sim 0$ and $z \sim 2.3$ is almost two

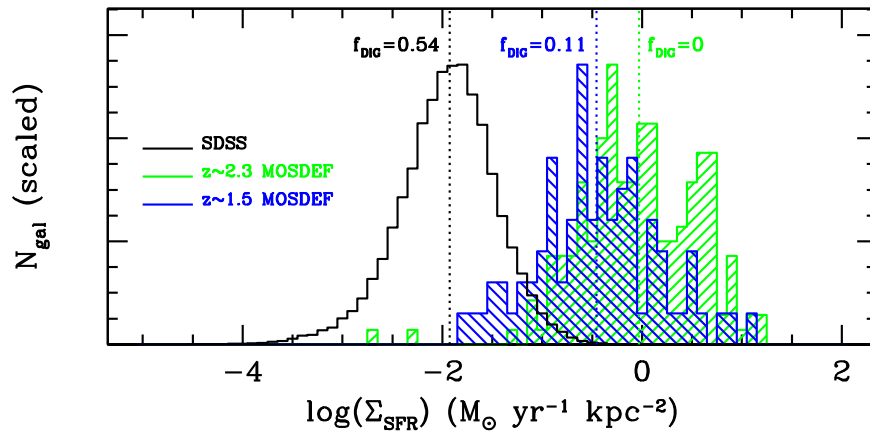


Figure 3. Σ_{SFR} distributions for SDSS and MOSDEF galaxies. The black histogram indicates the distribution in Σ_{SFR} for the $z \sim 0$ SDSS sample, while the shaded green [blue] histogram indicates the corresponding distribution for $z \sim 2.3$ [$z \sim 1.5$] MOSDEF galaxies. Equation (2) is used to translate the median Σ_{SFR} of each distribution to a corresponding f_{DIG} . While local star-forming galaxies typically have $f_{\text{DIG}} = 0.54$, the median Σ_{SFR} of $z \sim 2.3$ MOSDEF galaxies, which is almost two orders of magnitude higher, suggests $f_{\text{DIG}} = 0$.

orders of magnitude. We have also used Equation (2) to estimate the corresponding f_{DIG} value for each median Σ_{SFR} , finding median f_{DIG} values of 0.54, 0.11, and 0, for at $z \sim 0$, 1.5, and 2.3. For these calculations, we are making the simplifying assumption that the same relation between f_{DIG} and Σ_{SFR} holds at low and high redshift, although it has only been measured locally. If this assumption is valid, then the emission from the ionized ISM at $z \geq 1.5$ should be well represented by the ensemble-averaged emission of H II regions, with minimal (or zero, in the case of $z \sim 2.3$) contribution from DIG. This difference in the relative contributions of H II regions and DIG must be accounted for when interpreting the [S II] BPT diagram of high-redshift galaxies.

3.4. Revisiting the High-redshift [S II] BPT Diagram

In order to infer the differences between low- and high-redshift star-forming regions, we need to consider low- and high-redshift samples with the same f_{DIG} . For $z \sim 2.3$ MOSDEF galaxies, the appropriate comparison sample is either local H II regions, or the *hiionly* model of Sanders et al. (2017), with $f_{\text{DIG}} = 0$. Given the slightly lower Σ_{SFR} and higher inferred f_{DIG} for the MOSDEF $z \sim 1.5$ sample, we generated a model with $f_{\text{DIG}} = 0.11$ for the purposes of comparison, based on the methodology of Sanders et al. (2017). Figure 4 shows the [S II] BPT diagrams for the $z \sim 2.3$ and $z \sim 1.5$ MOSDEF samples of individual detections, along with the appropriate comparison models. The high-redshift MOSDEF samples are clearly shifted toward higher [S II] $\lambda\lambda 6717, 6731/\text{H}\alpha$ and [O III] $\lambda 5007/\text{H}\beta$ relative to the low-DIG comparison models, with a larger positive shift for the $z \sim 2.3$ sample.

4. Discussion

Previous comparisons between high-redshift and local SDSS galaxies in the [S II] BPT diagram suggested that there was zero or *negative* shift in [S II] $\lambda\lambda 6717, 6731/\text{H}\alpha$ at fixed [O III] $\lambda 5007/\text{H}\beta$. Such results led Shapley et al. (2015) to conclude that differences existed between low- and high-redshift N/O versus O/H abundance patterns, and Kashino et al. (2017) to infer higher ionization parameters at fixed nebular abundance. However, such analyses did not use the appropriate $z \sim 0$ comparison sample with minimal f_{DIG} . Our revised comparison

in the [S II] BPT diagram between high-redshift galaxies and local H II regions, or galaxies with minimal DIG contribution, demonstrates definitively that $z \geq 1.3$ galaxies have significant positive x - and/or y -offsets relative to their appropriate local counterparts in both the [N II] and [S II] BPT diagrams. Sanders et al. (2016) showed that, compared to a fiducial set of photoionization models, those with harder ionizing spectrum at fixed metallicity lead to corresponding positive offsets in both [N II] and [S II] BPT diagrams. Steidel et al. (2016) proposed an underlying physical scenario for such behavior, according to which chemically young high-redshift galaxies exhibit α enhancement, with stellar Fe-based metallicities a factor of several lower than nebular oxygen-based metallicities. Our analysis shows that the [N II] and [S II] BPT diagrams of high-redshift galaxies can be jointly explained by the combination of a harder ionizing spectrum at fixed metallicity due to α enhancement, and a lower f_{DIG} , compared with local star-forming galaxies.

The evolving mixture of DIG and H II region emission has implications for both photoionization models and strong-line metallicity calibrations. For example, the photoionization models of Levesque et al. (2010) and Hirschmann et al. (2017) neglect a detailed treatment of the DIG contribution to integrated galaxy line ratios, and neither set of model grids overlaps the bulk of $z \sim 0$ galaxies that they aim to describe in the [S II] BPT diagram. In both cases, the model grids fall much closer to the locus of H II regions, and clearly require the addition of DIG emission to correctly describe local galaxies (Sanders et al. 2017). As for metallicity calibrations, the recently introduced “N2S2” indicator relates metallicity to a linear combination of $\log([\text{N II}]/[\text{S II}])$ and $\log([\text{N II}]/\text{H}\alpha)$ (Dopita et al. 2016). However, because it includes [S II], N2S2 is sensitive to *both* metallicity and f_{DIG} . Robust evolutionary comparisons between the integrated oxygen abundances of high- and low-redshift galaxies must be made using empirical indicators that are insensitive to variations in f_{DIG} .

Our conclusions are based on the assumption that high-redshift galaxies follow the same relationship between f_{DIG} and Σ_{SFR} that is observed in local galaxies (Oey et al. 2007). We now need to test our assumption of redshift invariance by constructing rest-optical emission-line maps of distant galaxies on sub-kpc scales, and measuring both f_{DIG} and Σ_{SFR} . Such observations will be possible with the integral-field unit (IFU)

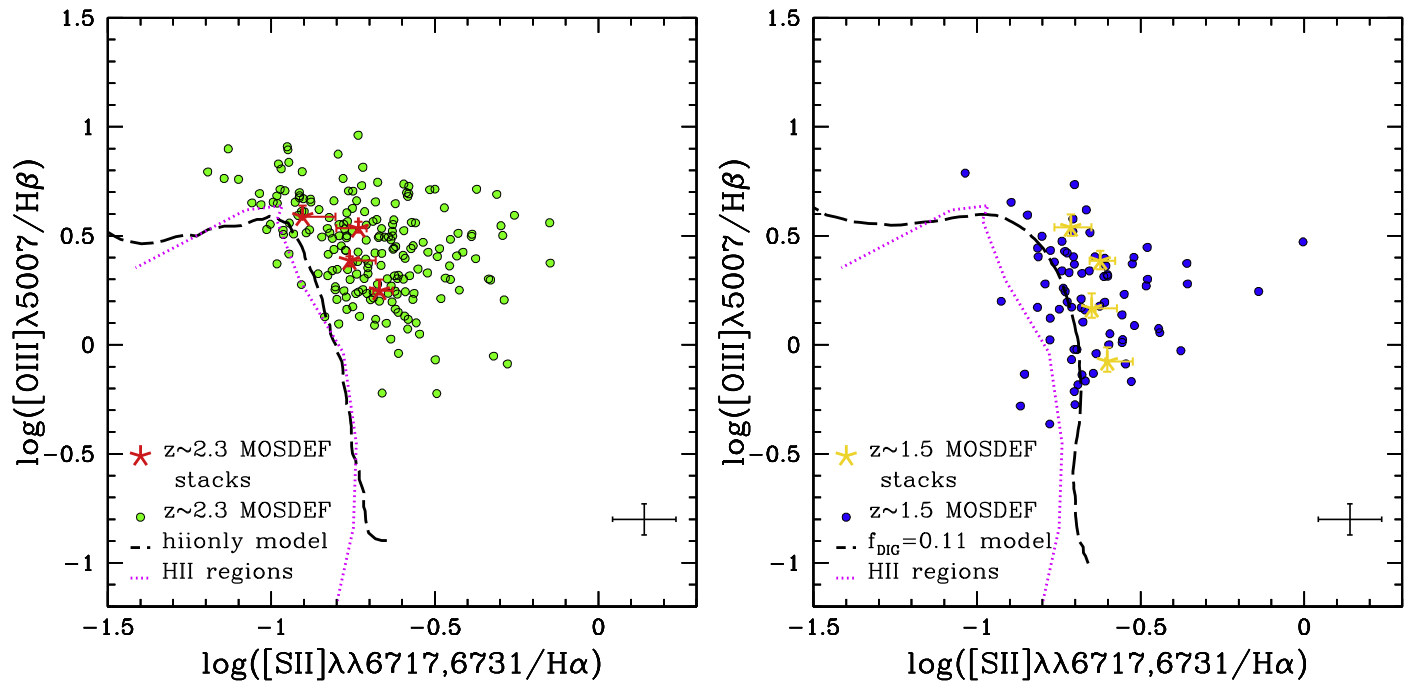


Figure 4. Comparison in the [S II] BPT diagram between MOSDEF galaxies, H II regions, and models with low DIG emission fraction. Left panel: [S II] BPT diagram for $z \sim 2.3$ MOSDEF galaxies and stacks (green points, red stars), median sequence of local H II regions (magenta dotted line), and *hiionly* model from Sanders et al. (2017; black dashed line). $z \sim 2.3$ MOSDEF galaxies are clearly offset toward larger [O III] λ 5007/H β and/or larger [S II] $\lambda\lambda$ 6717,6731/H α relative to local H II regions and the *hiionly* model. Right panel: the same plot, but for $z \sim 1.5$ MOSDEF galaxies and stacks (blue points, gold stars), local H II regions (magenta dotted line), and a model from Sanders et al. (2017) representing the ensemble average emission from H II regions in star-forming galaxies plus a DIG fractional contribution to the H α emission of $f_{\text{DIG}} = 0.11$. The offset between $z \sim 1.5$ MOSDEF galaxies and the comparison curves is smaller than for the $z \sim 2.3$ MOSDEF sample.

of the NIRSpect instrument aboard the *James Webb Space Telescope* and planned adaptive-optics-assisted IFUs on the next generation of extremely large ground-based telescopes.

We acknowledge support from NSF AAG grants AST-1312780, 1312547, 1312764, and 1313171, grant AR-13907 from the Space Telescope Science Institute, and grant NNX16AF54G from the NASA ADAP program. We also acknowledge a NASA contract supporting the “WFIRST Extragalactic Potential Observations (EXPO) Science Investigation Team” (15-WFIRST15-0004), administered by GSFC. We thank the 3D-*HST* collaboration, who provided us with spectroscopic and photometric catalogs used to select MOSDEF targets and derive stellar population parameters. We acknowledge the First Carnegie Symposium in Honor of Leonard Searle for useful information and discussions that benefited this work. We finally wish to extend special thanks to those of Hawaiian ancestry on whose sacred mountain we are privileged to be guests.

ORCID iDs

Alice E. Shapley <https://orcid.org/0000-0003-3509-4855>
 Ryan L. Sanders <https://orcid.org/0000-0003-4792-9119>
 Naveen A. Reddy <https://orcid.org/0000-0001-9687-4973>
 Mariska Kriek <https://orcid.org/0000-0002-7613-9872>
 Alison L. Coil <https://orcid.org/0000-0002-2583-5894>
 Brian Siana <https://orcid.org/0000-0002-4935-9511>
 Irene Shivaie <https://orcid.org/0000-0003-4702-7561>
 William R. Freeman <https://orcid.org/0000-0003-3559-5270>
 Mojegan Azadi <https://orcid.org/0000-0001-6004-9728>
 Sedona H. Price <https://orcid.org/0000-0002-0108-4176>

Gene C. K. Leung <https://orcid.org/0000-0002-9393-6507>
 Francesca M. Fornasini <https://orcid.org/0000-0002-9286-9963>
 Guillermo Barro <https://orcid.org/0000-0001-6813-875X>

References

- Abazajian, K. N., Adelman-McCarthy, J. K., Agüeros, M. A., et al. 2009, *ApJS*, 182, 543
 Azadi, M., Coil, A. L., Aird, J., et al. 2017, *ApJ*, 835, 27
 Baldwin, J. A., Phillips, M. M., & Terlevich, R. 1981, *PASP*, 93, 5
 Cardelli, J. A., Clayton, G. C., & Mathis, J. S. 1989, *ApJ*, 345, 245
 Chabrier, G. 2003, *PASP*, 115, 763
 Coil, A. L., Aird, J., Reddy, N., et al. 2015, *ApJ*, 801, 35
 Dopita, M. A., Kewley, L. J., Sutherland, R. S., & Nicholls, D. C. 2016, *Ap&SS*, 361, 61
 Freeman, W. R., Siana, B., Kriek, M., et al. 2019, *ApJ*, 873, 102
 Grogin, N. A., Kocevski, D. D., Faber, S. M., et al. 2011, *ApJS*, 197, 35
 Hao, C.-N., Kennicutt, R. C., Johnson, B. D., et al. 2011, *ApJ*, 741, 124
 Hirschmann, M., Charlot, S., Feltre, A., et al. 2017, *MNRAS*, 472, 2468
 Kashino, D., Silverman, J. D., Sanders, D., et al. 2017, *ApJ*, 835, 88
 Kashino, D., Silverman, J. D., Sanders, D., et al. 2019, *ApJS*, 241, 10
 Kauffmann, G., Heckman, T. M., Tremonti, C., et al. 2003, *MNRAS*, 346, 1055
 Kewley, L. J., Dopita, M. A., Sutherland, R. S., Heisler, C. A., & Trevena, J. 2001, *ApJ*, 556, 121
 Koekemoer, A. M., Faber, S. M., Ferguson, H. C., et al. 2011, *ApJS*, 197, 36
 Kriek, M., Shapley, A. E., Reddy, N. A., et al. 2015, *ApJS*, 218, 15
 Levesque, E. M., Kewley, L. J., & Larson, K. L. 2010, *AJ*, 139, 712
 Masters, D., Faisst, A., & Capak, P. 2016, *ApJ*, 828, 18
 Masters, D., McCarthy, P., Siana, B., et al. 2014, *ApJ*, 785, 153
 McLean, I. S., Steidel, C. C., Epps, H. W., et al. 2012, *Proc. SPIE*, 8446, 84460J
 Momcheva, I. G., Brammer, G. B., van Dokkum, P. G., et al. 2016, *ApJS*, 225, 27
 Oey, M. S., Meurer, G. R., Yelda, S., et al. 2007, *ApJ*, 661, 801
 Pettini, M., & Pagel, B. E. J. 2004, *MNRAS*, 348, L59
 Pilyugin, L. S., & Grebel, E. K. 2016, *MNRAS*, 457, 3678

- Reddy, N. A., Kriek, M., Shapley, A. E., et al. 2015, *ApJ*, 806, 259
- Sanders, R. L., Shapley, A. E., Kriek, M., et al. 2016, *ApJ*, 816, 23
- Sanders, R. L., Shapley, A. E., Kriek, M., et al. 2018, *ApJ*, 858, 99
- Sanders, R. L., Shapley, A. E., Zhang, K., & Yan, R. 2017, *ApJ*, 850, 136
- Shapley, A. E., Reddy, N. A., Kriek, M., et al. 2015, *ApJ*, 801, 88
- Skelton, R. E., Whitaker, K. E., Momcheva, I. G., et al. 2014, *ApJS*, 214, 24
- Steidel, C. C., Rudie, G. C., Strom, A. L., et al. 2014, *ApJ*, 795, 165
- Steidel, C. C., Strom, A. L., Pettini, M., et al. 2016, *ApJ*, 826, 159
- Strom, A. L., Steidel, C. C., Rudie, G. C., et al. 2017, *ApJ*, 836, 164
- van der Wel, A., Franx, M., van Dokkum, P. G., et al. 2014, *ApJ*, 788, 28
- Veilleux, S., & Osterbrock, D. E. 1987, *ApJS*, 63, 295
- Zhang, K., Yan, R., Bundy, K., et al. 2017, *MNRAS*, 466, 3217
- Zurita, A., Rozas, M., & Beckman, J. E. 2000, *A&A*, 363, 9